Electrochemically active novel amorphous carbon (a-C)/Cu$_3$P peapod nanowires by low-temperature chemical vapor phosphorization reaction as high efficient electrocatalysts for hydrogen evolution reaction

Arumugam Manikandan [a], Pavithra Sriram [a], Kun-Chieh Hsu [b], Yi-Chung Wang [a], Chia-Wei Chen [a], Yu-Chuan Shih [a], Ta-Jen Yen [a], Horng-Tay Jeng [b], Hao-Chung Kuo [c], Yu-Lun Chueh [a, d, e, *]

[a] Department of Materials Science and Engineering, National Tsing Hua University, Hsinchu 30013, Taiwan, ROC
[b] Department of Physics, National Tsing Hua University, Hsinchu 30013, Taiwan, ROC
[c] Department of Photonics and Opto-Electrical Engineering, National Chiao Tung University, Hsinchu 30010, Taiwan, ROC
[d] Frontier Research Center on Fundamental and Applied Sciences of Matters, National Tsing Hua University, Hsinchu 30013, Taiwan, ROC
[e] Department of Physics, National Sun Yat-Sen University, Kaohsiung, 80424, Taiwan, ROC

ARTICLE INFO

ABSTRACT

Toward finding low-cost electrocatalysts with high catalytic properties to replace noble metals as high efficient electrocatalysts in electrochemical hydrogen evolution reaction (HER) of total water splitting plays a vital role to approach the green and sustainable energy supply. Here, we demonstrate the direct growth of novel copper phosphide coated with amorphous carbon, namely heterostructured a-C/Cu$_3$P peapod nanowires from chemically synthesized copper nanowires (Cu NWs) followed by a chemical vapor phosphorization reaction (CVPR) process at a low temperature of $400\,^\circ$C. The heterostructured a-C/Cu$_3$P peapod nanowires exhibit a superior electrocatalytic activity by a lower overpotential of 287 mV at a current density of $10\,\mathrm{mA\,cm^{-2}}$ with a low Tafel slope of $72\,\mathrm{mV\,dec^{-1}}$ and excellent stability over 1000 cycles. The superior electrocatalytic performance can be explained by the superior contact of the electrolyte with active sites on the heterostructured a-C/Cu$_3$P due to the high surface area of peapod nanowire structure covered by defective edges of graphene with the encapsulated amorphous carbon layer, which can tremendously enhance electrical conductivity at the surface.

© 2019 Published by Elsevier Ltd.

1. Introduction

Hydrogen (H$_2$) has been considered as the superlative candidate to reduce our demand on fossil fuels and to overcome significant concerns such as environmental pollution, energy consumption and greenhouse effect. It is well known that water electrolysis is an efficient technique to produce a high yield of molecular H$_2$ assisted by an electrocatalyst. Therefore, it has been attracted much attention among other techniques such as coal gasification and steam methane reforming [1]. Platinum (Pt)-based materials are state-of-

the-art of hydrogen evolution reaction (HER) catalyst due to its high electrical conductivity and remarkable catalytic property. However, its scarcity and higher production cost limit its widespread usage [2]. Therefore, finding alternative electrocatalysts with earth abundant, low-cost and high catalytic property are imperative. Remarkable development on noble metal-free electrocatalysts such as transition metal dichalcogenides [3—8], carbides [9—11], nitrides [12] and metal-free catalyst [13] have been demonstrated recently. Besides, transition metal phosphides (TMPs) are highly conductive with high corrosion resistance, thus exhibiting an interesting catalytic activity [1]. Generally, TMPs are intensively used as an excellent catalyst in hydrodesulfurization reaction (HDS) due to its promising feature of reversible binding and dissociation of H$_2$ [14,15]. Similarly, HER work in the same way with H$^+$ cation bound to the catalyst to produce H$_2$ and it is construed that TMP

may be an active catalyst for HER. There have many efforts made in the past few years on the preparation of several TMPs as an electrocatalyst for HER such as molybdenum phosphides [16–18], nickel phosphides [19–22], cobalt phosphides [23–25], iron phosphides [26–28], and copper phosphides [29–34]. Because of rich redox properties and relatively low-cost due to its high earth abundance [35], Cu-based materials are being focused among other phosphides as an excellent electrocatalyst in overall water splitting (HER at cathode and oxygen evolution reaction (OER) at the anode). However, its poor resistance to acidic environments is of a significant challenge in higher H_2 productive electrolyte like H_2SO_4 in HER. To solve this major issue, in our previous work, we proposed the low-temperature growth of a graphene coating layer on Cu nanowires as a highly efficient and acid stable electrocatalyst [36]. Likewise, several reports based on transition metal sulfides (ex. MoS_2) states that the coating of carbon-based materials enriches the electrical conductivity and improves the stability over acidic electrolytes [37,38]. Therefore, a coating layer of carbon-based materials can be considered as one of the main strategies to improve catalytic activity and stability. On the other hand, by integrating Cu with phosphorous (P), leading to the formation of distinctly metallic character, both elements contribute equally in HER, which facilitate fast charge transfer, thus accelerating HER kinetics. For example, C.C.Hou et al. have prepared binder free self-supported Cu_3P on a copper foam and reported that the Cu atoms favor for adsorption of OH^- from the decomposition of water while P atoms will combine H atoms [31]. In addition, subsequent development toward creating nanostructures are imperative, leading to the easy diffusion of electrolytes toward active sites of the catalyst.

Therefore, it is conceivable to apply the following strategies to Cu-based HER catalyst to improve the intrinsic activity including the integration with P to fasten electron transfer with high conductivity [31], coating of carbon layer to improve stability in the acidic electrolyte [32] and nanostructure to improve easy diffusion of electrolyte towards active sites [4]. Keeping these strategies in mind, in this work, the fabrication of the amorphous carbon (a-C) coated on Cu_3P peapod nanowires (NWs) synthesized by low-temperature chemical vapor phosphorization reaction (CVPR) method on a conductive substrate as highly effective HER electrocatalysts was demonstrated. The CVPR is of the particular interesting process, providing selectivity of non-toxic precursor [39], composition controllability, non-tedious processing and low-temperature synthesis ability compared to chemical phosphorization and chemical vapor deposition (CVD) [40,41]. First, we coated a-C on chemically synthesized Cu nanowires followed by the phosphorization at a low temperature of 400 °C to obtain Cu_3P. Then, we directly use this heterostructured a-C/Cu_3P peapod NWs as the HER electrode without any binder, which makes it as the binder-free electrocatalyst. The coated a-C layer on Cu_3P peapod NWs not only acts as a protective layer over acidic electrolyte but also improves the conductivity. Therefore, the heterostructured a-C/Cu_3P peapod NWs offer a lower overpotential of 287 mV at the current density of 10 mAcm^{-2} and a lower Tafel slope of 72 mVdec^{-1} with high stability over 1000 cycles. A theoretical study at the active sites of heterostructured a-C/Cu_3P peapod NWs by density functional theory (DFT) was proposed. Finally, how the importance of the coated a-C layer and Cu_3P peapod NWs were addressed, paving a feasible way to prepare an inexpensive, catalytically active and highly stable electrocatalyst for the production of excessive H_2 via the electrochemical water splitting process.

2. Experimental methods

2.1. Synthesis of copper nanowire

102 mg Nickel acetylacetonate (Acros Organics), 136 mg copper (II) chloride dihydrate (showa) and 10 ml oleylamine (Aldrich) were stirred continuously in a 50 ml round bottom flask at 80 °C with a high rpm for 30 min. Subsequently, the temperature was raised to 180 °C and continued for 10 h without stirring and cool down to room temperature. Finally, the solution was washed several times with excess hexane and acetone simultaneously followed by the centrifugation at 8000 rpm for 10 min and dried in air overnight.

2.2. Formation of heterostructured a-C/Cu_3P peapod nanowires by CVPR

As-prepared Cu NWs with the concentration of 1 mg/ml were vacuum filtered on a nitrocellulose membrane and transferred onto a 50 nm-thick gold (Au) coated layer on a SiO_2/Si substrate. Initially, the residual carbon coated on Cu NW was transferred to the amorphous carbon by the pre-annealing process under a reduced H_2 gas with 100 sccm at 200 °C for 1 h. In addition, the residual nitrocellulose membrane on the Cu NW network also acts as the additional feedstock of carbon. Then, 500 mg of sodium hypophosphite was placed at the upstream of the furnace tube with a distance of 5 cm from the annealed Cu NWs for the phosphorization reaction. Moreover, the parameters were tuned by setting up the temperature from 300 °C to 500 °C, reaction time from 30 to 90 min and a carrier gas such as air, H_2, and argon (Ar). The optimized growth parameter is at the base pressure of 1×10^{-3} Torr at 400 °C for 60 min in the presence of H_2 of 100 sccm and the furnace was cooled rapidly.

2.3. Formation of Cu_2P/Cu_3P nanowires by the CVPR

The transferred CuNWs were directly phosphorized at the same parameters without pre-annealing nanowires. Sodium hypophosphite (500 mg) was placed in a quartz boat in the furnace and the base pressure was maintained at 1×10^{-3} Torr at 400 °C in the presence of H_2 for an hour.

2.4. Synthesis of red phosphorous

Sodium hypophosphite (500 mg) was placed in a quartz boat in the furnace and the base pressure was maintained at 1×10^{-3} Torr at 400 °C in the presence of H_2 for an hour. Then sample was collected as powder and deposited on a glass substrate for further analysis.

2.5. Material characterizations

Surface morphologies of samples were observed by field-emission scanning electron microscopes (FE-SEM, Hitachi, SU8010). Crystal structure and quality were verified and confirmed by Raman spectroscopy (HORIBA Jobin-Yvon, LabRAM, HR800) equipped with 532 nm laser and X-ray diffraction (Shimadzu XRD-6000, Cu Kα, λ = 0.154 nm) with scanning angles from 15 to 65°. The lattice spacing of the samples was analyzed by a high-resolution transmission electron microscope (HRTEM; JEM-F200 FEGTEM, JEOL, Japan) operated at 200 kV with the point-to-point resolution of 0.17 nm. X-ray photoemission spectroscopy (XPS)

with a monochromatic Al Kα X-ray source (XPS, Ulvac-PHI 1600) were utilized to the evidenced presence of surface carbon coating.

2.6. Measurements of electrochemical hydrogen evolution reaction

The electrochemical measurements were performed in a three-electrode system using a Bio-Logic VSP potentiostat in a cylindrical cell made of Teflon with an O-ring at the bottom area of 0.212 cm^2. The electrochemical impedance spectra were recorded from 0.1 Hz to 100 kHz at an amplitude of 10 mV. A Pt wire, graphite rod and Ag/AgCl (3M NaCl) were used as the counter and reference electrodes, respectively. The prepared samples were connected using 3M copper tape and were used as the working electrode. In addition, 5 mg of commercially available Pt/C (Aldrich), which was mixed with ethanol and coated onto Au coated SiO$_2$/Si substrate, was protected using a Nafion coating (10 μl) for the comparison. For all the measurements, 0.5 M H$_2$SO$_4$ and KOH were used as an electrolyte. All potentials were converted to potentials concerning Reversible Hydrogen Electrode (RHE) by using the equation $E_{RHE} = E_{Ag/AgCl} + 0.0591 \times pH + 0.194$, resulting in a shift of −0.2117 V *vs.* RHE. Note all potentials in linear sweep voltammetry (LSV) were collected after applying 3–5 potential sweeps in order to avoid the redeposition of Pt on the working electrode after several cycles and reported vs RHE without *i*R compensation. Cyclic voltammetry was acquired in a non-faradaic region between 0.05 and 0.16 V (vs RHE) at various scan rates (5–400 mV s^{-1} vs RHE) to evaluate the double layer capacitance (C$_{dl}$). The stability was examined by continuously cycling potentials between +0.2 and −0.6 V at a scan rate of 5 mV s^{-1}.

2.7. Theoretical calculation using density functional theory

The DFT calculation was performed by Vienna Ab initio Simulation Package (VASP) [42] by the projector augmented wave method (PAW) [43] as a pseudopotential and the pedew-Burke-Ernzerhof (PBE) [44] as an exchange-correlation function. The energy changes under different coverages of hydrogen atoms were studied on a surface unit with a cell size of (2 × 2). The cells were not repeated in z-direction so that only three slabs can be observed. Note that we have fixed the bottom layer and allowed the other two layers in varied conditions. Each slab has a 1 nm above the vacuum layer. Moreover, (9 × 9 × 1) gamma centered Monkhorst-Pack k-points [45] and Brillouin-zone integration was performed by the Tetrahedron method with Blochl corrections, respectively [46]. In addition, cut-off energy for the plane wave basis was set at 270 eV without the spin polarization.

3. Results and discussion

As schematically illustrated in Fig. 1(a), the combination of vacuum filtration of Cu NWs on nitrocellulose membrane followed by transferring Cu NWs into substrates, annealing Cu NWs under a reductive hydrogen atmosphere and a chemical vapor phosphorization reaction (CVPR) are important processes to achieve heterostructured a-C/Cu$_3$P peapod NWs. First, the Cu NWs were synthesized by the chemical reduction of copper chloride in assistance with oleylamine as a reductive agent and nickel acetylacetonate as a catalyst at 180 °C (see experimental section for details). The as-prepared Cu NWs were 80–120 nm in diameter and several micrometers in length as shown in Figure S1a, with which the CuO dots forms in the residual carbon layer denoted as a-CuO (Figure S1b). The removal of the a-CuO and the uniform coating of amorphous carbon (a-C) layer can be successfully achieved after annealed in the presence of H$_2$ as shown in Figures S1c and d, denoted as a-CuNW. Figure S1(e) displays the Raman spectra of the

annealed Cu nanowire (a-CuNW) in comparison with as-prepared Cu NWs measured at the excitation wavelength of 532 nm in order to evaluate the importance of the annealing process to achieve the a-C coating layer on Cu NWs. Typical D and G bands of the amorphous carbon located at 1397 and 1583 cm^{-1} can be measured [47]. The appearance of both D and G bands at the a-CuNW signifies that the a-C coating layer is successfully grown after the annealing process. To achieve specific peapod nanostructure on a-C-coated Cu NWs, the growth temperature, reaction time and a carrier gas of chemical vapor phosphorization reaction (CVPR) have to be optimized.

At first, the carrier gas (H$_2$) and the phosphorized time (60 min) were fixed with phosphorized temperatures varied from 300 to 500 °C and corresponding SEM images are shown in Fig. 1(b) to 1(d) denoted as a-C/Cu$_3$P@ 300 °C, a-C/Cu$_3$P@ 400 °C and a-C/Cu$_3$P@ 500 °C, respectively. The crystalline structures of samples with different phosphorized parameters were characterized by X-ray diffraction spectrometer as shown in Fig. 1(e). For the a-Cu NWs, the observed characteristic peaks of single crystalline Cu (JCPDS 03–1005) with face-centered cubic (FCC) structure at 43.4, 50.6 and 74.3°, corresponding to (111), (200) and (220) planes were found, respectively. A phase transformation process occurs at the phosphorization temperature of 300 °C, with which the phase of Cu$_3$P with a hexagonal structure (PDF# 02–1623) in all diffraction peaks at 28.4°, 36.1°, 39.2°, 41.5°, 45°, 46.2°, 47.3°, 52.2°, 53.5°, 56.6°, 59°, 66.6°, 69.2°, 73.5° and 78.3° corresponding to the (111), (112), (202), (211), (300), (113), (212), (220), (221), (311), (222), (223), (321), (322) and (314) crystalline phases can be confirmed, respectively. No other peaks exist, which indicate the pure phase of Cu$_3$P in all phosphorized temperatures (300, 400 and 500 °C in our current study) [30] Furthermore, a broad peak located at 23° corresponding to (002) plane indicates the formation of the graphitic carbon layer in three different phosphorized samples [48]. Although there is no difference in the phase of Cu$_3$P for samples at three different phosphorized temperatures, the morphologies are quite different at different phosphorized temperatures. At the phosphorized temperature of 300 °C (a-C/Cu$_3$P@ 300 °C), the average diameter increases from 80 to 240 nm as shown Fig. 1(b), confirming that the partial phosphorization occurs. As the phosphorized temperature increases to 400 °C (a-C/Cu$_3$P@ 400 °C), the formation of the peapod shape can be observed due to severe phosphorization reaction as shown in Fig. 1(c) and its obvious changes in its diameter is evidenced as shown in Fig. S2. Successive increase in the phosphorized temperature to 500 °C (a-C/Cu$_3$P@ 500 °C), which is close to the melting point of Cu, leads to the aggregated structure due to a melting feature occurred on Cu NWs as shown in Fig. 1(d) [36]. Furthermore, the fixed phosphorized temperature of 400 °C with the same flux of carrier gas (H$_2$) was conducted at the different phosphorized time of 30 and 90 min to shed light on morphology changes. Distinctly, smaller bead-like nanostructures can be observed at the short reaction time (30 min) (Fig. S3a) and tend to consecutively increase its periodicity in peapod structure with an increase in the phosphorized time as shown in Fig. 1(c) for 60 min and Figure S3(b) for 90 min cases, respectively. Note that the aggregation of peapods in the phosphorized time of 90 min occurs because of high surface energy between peapods [49]. Eventually, the optimized phosphorization time (60 min) and temperature (400 °C) were found where the carrier gas was changed to air and argon (Ar). The absence of peapods on the Cu NW could be identified from Figure S3(c), indicating that the presence of the air ambient in CVPR is non-reactive. Moreover, in the presence of Ar, Cu NWs were reactively etched as shown in Figure S3(d). Therefore, the optimized growth parameters to achieve the peapod shape is 400 °C in the presence of H$_2$ as carrier gas at 60 min, respectively, which was used for further
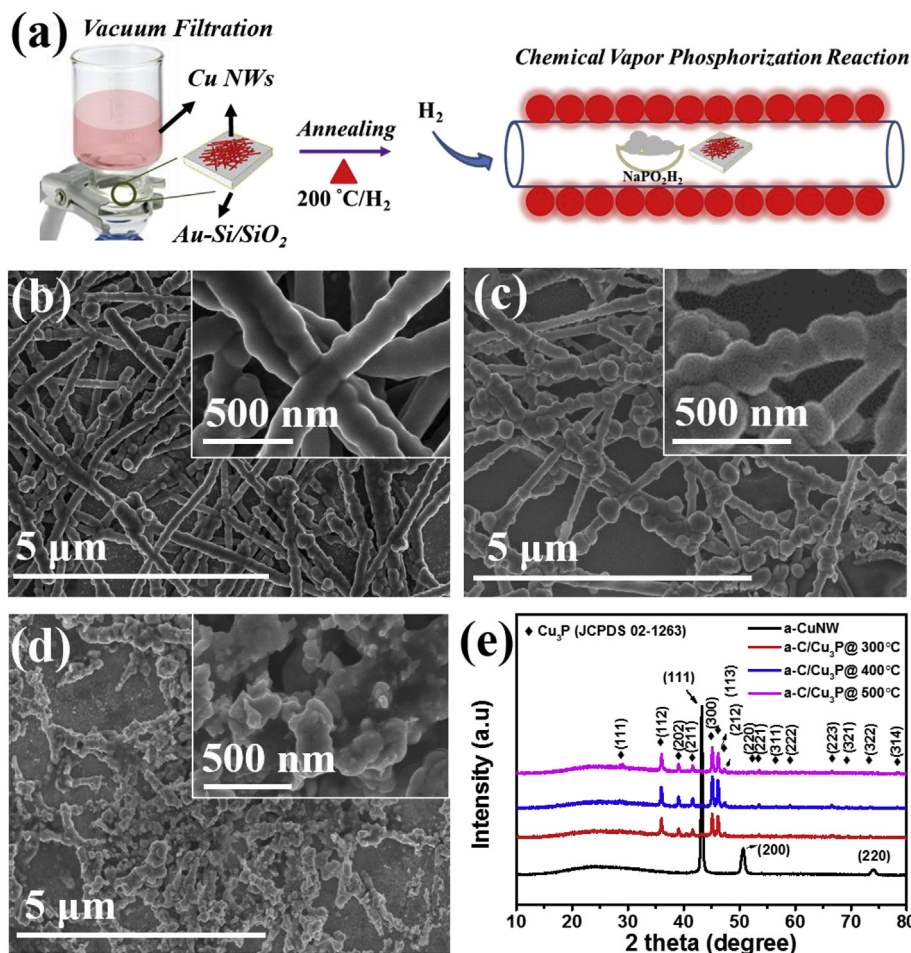
Fig. 1. (a) Schematic of heterostructured a-C/Cu₃P peapod NWs by the low-temperature chemical vapor phosphorization reaction. (b–d) SEM images of a-C/Cu₃P @ 300 °C, a-C/Cu₃P @ 400 °C and a-C/Cu₃P @ 500 °C and (e) the corresponding XRD results in comparison with a-CuNW.

analysis.

A transmission electron microscopy (TEM) image of a-C/Cu₃P@ 400 °C as shown in Fig. 2(a) further confirms the peapod morphology where the inner core of the peapod consists of the hollow structure indicated by dotted yellow lines. An amorphous carbon layer with a thickness of ~8 nm coated by ~6 graphene layers can be observed by the high-resolution TEM (HRTEM) image as shown in Fig. 2(b). In addition, the clear crystal plane can be observed with a lattice spacing of 0.208 nm, confirming the crystallinity of Cu₃P, which is consistent with XRD results [34,50]. Moreover, energy dispersive X-ray spectroscopy (EDS) line scan mapping across the peapod structure was conducted to obtain its chemical compositions. Interestingly, the surface, which is mainly composed of Cu, P and C, were uniformly distributed throughout the nanowire as shown in Fig. 2(c) and its quantitative elemental results are present in Figure S4. These findings strongly confirm that the core of a-C/Cu₃P@ 400 °C peapod NW is completely hollow. Furthermore, the graphene layer and degree of defects in a-C/Cu₃P@ 400 °C were investigated by Raman spectroscopy as shown in Fig. 3(a). The Raman spectra recorded at the excitation wavelength of 532 nm clearly shows typical weak D band at 1358 cm^{-1} and strong G band at 1588 cm^{-1} confirm the existed graphene coating layer. Where G band arises from the stretching mode of the C–C bond to all sp^2 carbon systems and the D band is caused by the disorder of the sp^2 hybridized carbon, respectively [51]. In addition, the peak shifts and the disappearance of the 2D peak, as well as the

ratio of I_D/I_G being 0.85, can be found due to the curved morphology of peapod NWs, indicating the carbon layer with the rich amorphous structure, which is consistent with results from XRD and TEM [36,47,52]. Except these two peaks, the other Raman peaks at range 100–600 cm^{-1} are the characteristic peak of the Cu₃P [53]. To emphasize the reaction between phosphorous powders and copper, we prepared red phosphorous (see experimental section for details) and compared with commercially available amorphous red phosphorous by Raman spectroscopy. Figure S5 shows Raman spectra of a-C/Cu₃P@ 400 °C (magnified at 100-600 cm^{-1} from Fig. 3(a)) in comparison with as prepared red phosphorous (Red P@400 °C) and commercial amorphous red phosphorous. The Raman spectra observed for Red P@400 °C are well matched with commercial Red-P [54,55] and an increased intensity of peak located at 350 cm^{-1} can be observed, which corresponds to P₉ cage, which is mostly responsible for forming pentagonal tubes in paired layers in amorphous red phosphorus [55]. Note that the a-C coated copper nanowires also react with the phosphorous vapor result in the suppression of amorphous peak at 350 cm^{-1}, leading to the formation of a strong and sharp peak at 424 cm^{-1}, strongly confirming the formation of Cu₃P [53].

X-ray photoemission spectroscopy (XPS) was conducted to gain more insights into the chemical state and composition of an individual element in the synthesized a-C/Cu₃P@ 400 °C. For comparison, XPS spectra at the surface of peapod NWs were measured by etching the conformal coating of the a-C by Ar ions. The
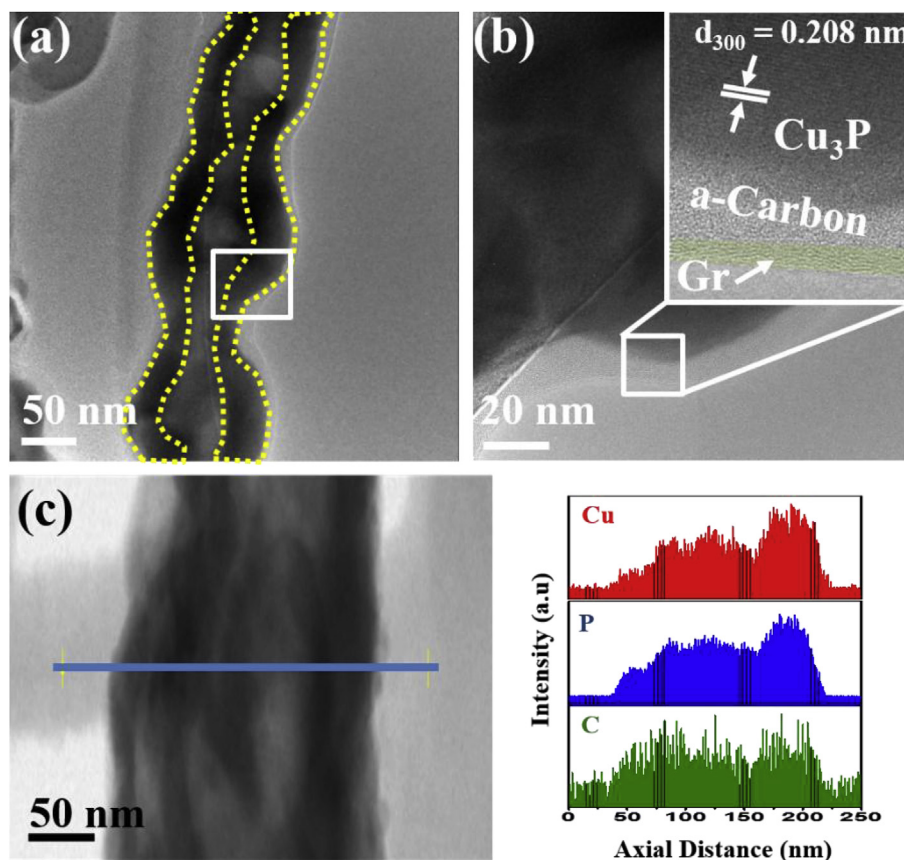
Fig. 2. (a) Low and (b) High magnification TEM images of a-C/Cu$_3$P @ 400 °C. (c) Shows the corresponding EDS line scan mapping profiles with Cu, P and C elements.

corresponding XPS results are shown in Fig. 3(b) where core level spectra of C1s representing sp^2 and sp^3 hybridized states in lower binding energies at 284.3 and 285.1eV on the surface of a-C/Cu$_3$P@ 400 °C were found. After the etching process of 6 S, the relative intensity of peaks decreases and broadens with a slight shift of peaks from 284.3 to 284.5 eV and 285.1—285.4 eV, respectively, confirming that the removal of the graphene layer from the surface of the thick carbon layer [56]. Fig. 3(c) shows the core level spectra of Cu 2p for the same condition with and without the etching process. The peaks at 932.6 and 952.3 eV, corresponding to Cu 2p$_{3/2}$ and Cu 2p$_{1/2}$, indicate oxidation state of Cu^{1+} (Cu$^{\delta+}$ of Cu$_3$P). The signal from high-energy peaks at 934.8 and 954.6 eV correspond to the oxidation state of Cu^{2+} and the peak at 943.4 eV attributes to the satellite peak of Cu 2p$_{3/2}$ from the surface of peapod NWs, respectively [30,57]. After the etching process, the oxidized species cannot be observed while two distinct peaks with slight shifts correspond to the Cu 2p$_{3/2}$ and Cu 2p$_{1/2}$ at 932.9 and 952.7 eV of Cu$_3$P, strongly confirming the growth of pure Cu$_3$P as the core of peapod NWs [30,58]. In P 2p peaks as shown in Fig. 3(d), two types of P species were found at before and after the etching process. The peak at 129.4 eV belongs to P$^{\delta-}$ in the metal phosphides corresponding to P 2p$_{3/2}$, and the peaks at 133.2 eV and 134.1 eV can be assigned to P 2p$_{1/2}$ and the oxidization state of P species (PO$_4^{3-}$), respectively. Besides, the observed increase in intensity after the etching process denotes the formation of Cu$_3$P in the core and it is distinctly identified that the P termination of Cu$_3$P is mostly bound to C species at the outer most surface of peapod NWs [30,59].

Based on the discussion above, a possible mechanism for the growth of heterostructured peapod NWs by the CVPR was proposed as shown in Fig. 3(e). In the initial, the removal of the a-CuO

layer can be achieved after the annealing of Cu NWs in the H$_2$ reductive ambient because of high H$_2$ solubility in Cu, leading to the change of residual carbon to the amorphous carbon as shown in Fig. 3(e$_1$) and 3(e$_2$). Here, H$_2$ plays an important role as reducing agent to proceed not only the etching process indicated by the bright arrow but also being as the chemical adsorber reacting with residual carbon to transform to the a-C layer (Fig. 3e$_3$) [60]. After the successful growth of the a-C layer on Cu NWs, the CVPR was carried out. During this stage, H$_2$ carries PH$_3$, which was decomposed from the phosphorous source (sodium hypophosphate) at a temperature above 300 °C [61] and adsorbed on Cu NW due to its high adsorption ability with Cu, leading to the purely chemical reaction between phosphorous and Cu (Fig. 3e$_4$). Once the temperature reaches to 400 °C, Cu catalyzes PH$_3$ into elemental P atoms [32,55] followed by the diffusion of PH$_3$ atoms through a-C layer by the internal diffusion of H$_2$ (indicated by the bright arrows in Fig. 3e$_5$). In addition, recrystallization of a-C in the presence of Cu catalyst assisted with H$_2$ at this temperature results in the formation of few-layer graphene. However, due to the insufficient reaction temperature, the partial transformation of a-C is achieved as a few graphene layers at its surface. A few graphene layers combined with the a-C layer on Cu NWs will slow down the diffusion of P atoms, resulting in larger nuclear sites of Cu$_3$P crystals after the chemical reaction between Cu and P (Fig. 3e$_5$). Finally, hybrid graphene and a-C layers prevent lateral growth and out-diffusion of H$_2$ may trigger the formation of the hollow configuration, resulting in the formation of the a-C/Cu$_3$P peapod NWs as shown in Fig. 3(e$_6$) [62]. Here, we strongly believe the uniform a-C coating layer throughout NWs protects the peapod nanostructure during the out-diffusion process and remains it as stable heterostructure
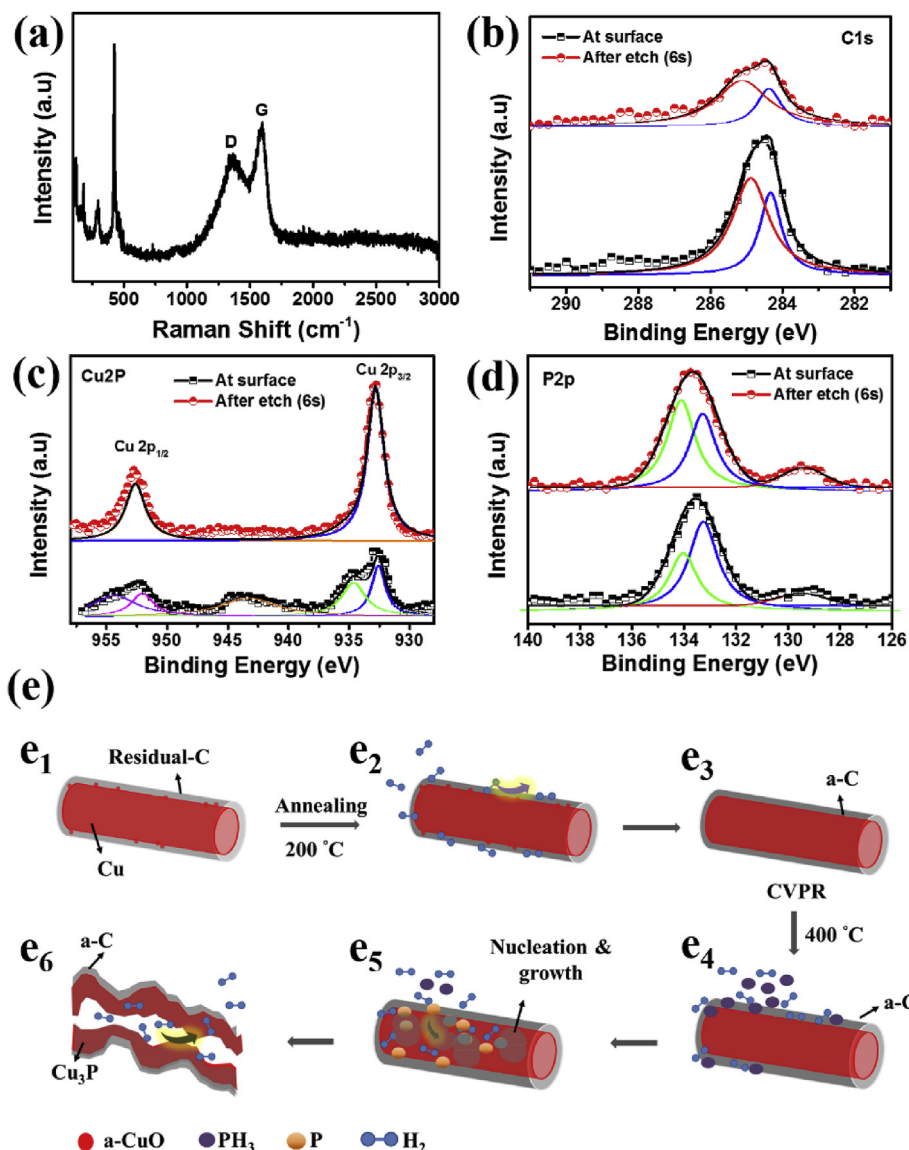
Fig. 3. (a) Raman spectra. XPS spectra of (b) C1s, (c) Cu 2p and (d) P 2p of a-C/Cu$_3$P @ 400 °C. (e) Schematics illustration at different growth stages of the peapod NWs.

peapod nanowire. To evaluate those phenomena, Cu NWs were phosphorized at the optimized parameter by CVPR without the coating of the a-C layer. Fig. S6(a) shows irregularly aggregated morphology after the phosphorization of Cu NWs and the corresponding XRD spectrum represents the formation of both Cu$_3$P and CuP$_2$ phases as shown in Fig. S6(b). The peaks at 22.1° (011), 25.3° (002), and 30.7° (−112) are the characteristic peaks of the CuP$_2$ phase (JCPDS 18−0452) [63] while rest of peaks are contributed from the Cu$_3$P phase (JCPDS 02−1623) [30]. The reaction of a-CuO presented on Cu NW with P atoms in CVPR results in the formation of CuP$_2$ nanoparticles. Additionally, the low and high magnification TEM images confirm the breakage of nanowires at the surface (indicated by a yellow dotted line) with the hollow configuration at the core region. However, due to the absence of a-C, it results in the formation of a non-peapod structure with CuP$_2$ nanoparticles on the Cu$_3$P shell layer (Figs. S6c and S6d). Obviously, a few graphene layers with the internal spacing of 0.358 nm were also obtained due to the crystallization of residual carbon on Cu NWs. Therefore, it is distinctly and directly evidenced that the a-C coating layer by the annealing process on Cu NWs plays an important role to achieve

heterostructured a-C/Cu$_3$P peapod NWs.

Considering the existence of highly chemical resistance to acidic electrolyte with high conductance because of a few graphene layers as well as easy contact of electrolyte towards active site because of the peapod morphology, an excellent hydrogen evolution reaction (HER) performance is strongly expected using a-C/Cu$_3$P as the catalyst. In a typical test, HER activity is evaluated by performing linear sweep voltammetry (LSV) in a 0.5 M H$_2$SO$_4$ electrolyte with a scan rate of 5 mV s^{-1} at room temperature. As shown in Fig. 4(a), the a-C/Cu$_3$P@ 400 °C catalyst exhibits much superior performance to the a-Cu NW, although the commercial Pt/C catalyst shows the best HER activity with the lowest onset potential and largest current density. Even after being phosphorized at 300 °C, the HER performance of a-C/Cu$_3$P@ 300 °C is still much better than that of a-Cu NWs. Thus, the overpotential can be reduced to 333 mV and 287 mV at the current density of 10 mA cm^{-2} for a-C/Cu$_3$P@ 300 °C and a-C/Cu$_3$P@ 400 °C compared with that of a-Cu NW (361 mV), respectively. Furthermore, a-C/Cu$_3$P@ 500 °C, which requires a higher overpotential of 402 mV to facilitate H$_2$ at the same current density, indeed shows the poor catalytic activity due to the damage
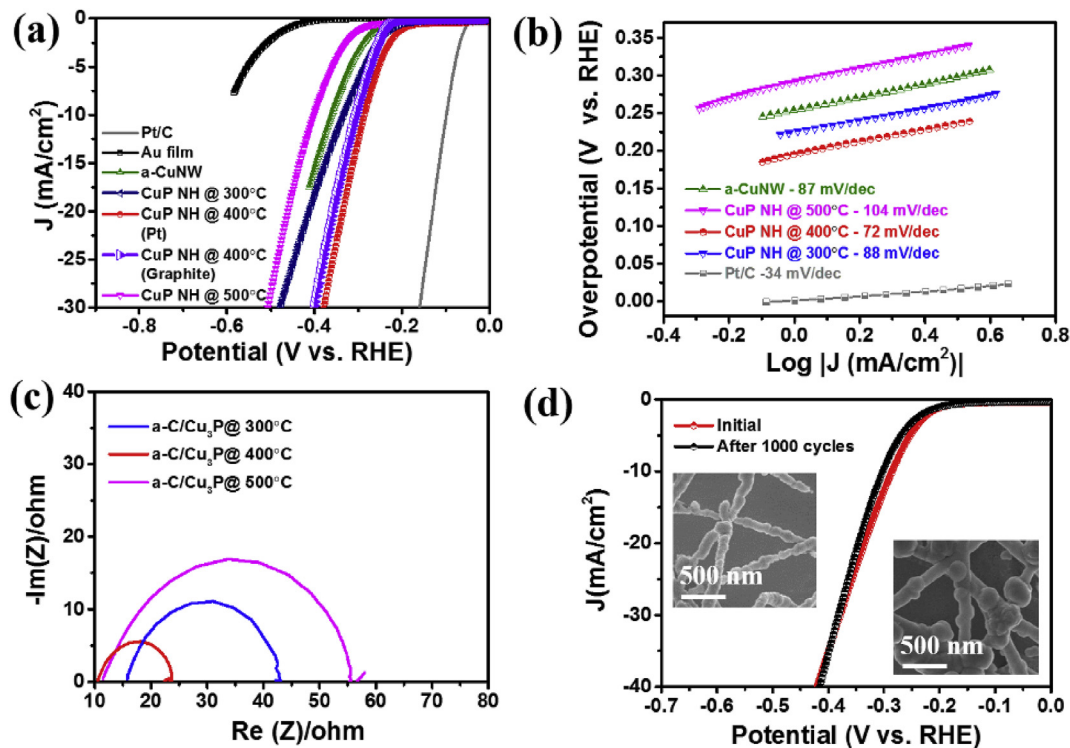
Fig. 4. (a) LSV polarization curves measured in 0.5 M H$_2$SO$_4$ at the scan rate of 5 mV s^{-1} for a-C/Cu$_3$P @ 300 °C, a-C/Cu$_3$P @ 400 °C and a-C/Cu$_3$P @ 500 °C in comparison with Pt/C, a-Cu NW and Au film, respectively. (b) Tafel plots from the corresponding LSV polarization curves of a-Cu NW, a-C/Cu$_3$P @ 300 °C, a-C/Cu$_3$P @ 400 °C and a-C/Cu$_3$P @ 500 °C, respectively. (c) Nyquist plots and (d) stability results from LSV over 1000 cycles for a-C/Cu$_3$P @ 400 °C in 0.5 M H$_2$SO$_4$ at the scan rate of 5 mV s^{-1}. Insets show the corresponding SEM images without the LSV polarization and the LSV polarization after the 1000th cycle.

of NWs. In contrast, the a-C/Cu$_3$P@ 400 °C sample revealed improved catalytic activities with negligible variation in performance using Pt and graphite as counter electrodes. Furthermore, the electrochemical performance of a-C/Cu$_3$P@ 400 °C in 0.5 M KOH was further investigated, showing the significant catalytic activity compared with that of Cu NW. Clearly, the a-C/Cu$_3$P@ 400 °C electrode required an overpotential of 554 mV compared to that of Cu NW (749 mV) at the current density of 10 mA cm^{-2} (Fig. S7). The polarization curves are replotted into Tafel plots by the Tafel equation ($\eta = a + b \log j$ where b is the Tafel slope and j is the current density). The slope of the linear fitting dominates the rate determining steps of HER, reflecting the inherent nature of electrocatalysts. Typically, for the HER in an acidic media, the adsorbed H ions formed on the active sites in the discharge step are the determinative step, leading to the Tafel slope >120 mV dec^{-1}, with which the rate-determining step follows Volmer reaction [64]. However, if the desorption step restricts the reaction, the Tafel slope between 40 and 120 mV dec^{-1} can be achieved where Heyrovsky reaction is the rate-determinative step [65]. By contrast, the reaction occurs through recombination of two adsorbed hydrogens. The rate-determining step will be dominated by Tafel reaction, with which the Tafel slope <40 mV dec^{-1} can be achieved [36]. As a result, Tafel plots depicted in Fig. 4(b) show a small Tafel slope of 72 mV dec^{-1} for a-C/Cu$_3$P @ 400 °C, which is lower than that of 87, 88 and 104 mV for a-Cu NW, a-C/Cu$_3$P @ 300 °C and a-C/Cu$_3$P @ 500 °C, respectively. The lower Tafel slope implies the superior catalytic property for the Cu$_3$P NH @ 400 °C, which is comparable and much better than that for reported phosphide-based electrocatalystes as shown in Table 1. As a result, the achieved lower Tafel slope of the Cu$_3$P NH @ 400 °C suggests that the Volmer-Heyrovsky dominates the electrochemical HER process. To further shed light on the kinetics of electrode, electrochemical impedance

spectroscopy (EIS) analysis was performed. As can be seen from Fig. 4(c), Nyquist plots show that the a-C/Cu$_3$P @ 400 °C has smaller charge transfer resistance than that of a-C/Cu$_3$P @ 300 °C and a-C/Cu$_3$P @ 500 °C, exhibiting the faster Faradaic process with the better HER kinetics. The smaller charge transfer resistance indicates that the presence of conductive amorphous carbon enriches the electrical conductivity of the Cu$_3$P [37]. Moreover, stability is one of the significant issues to evaluate the performance of electrocatalyst. Fig. 4(d) denotes the LSV measured at the scan rate of 5 mVs^{-1} for a-C/Cu$_3$P @ 400 °C over 1000 cycles, with which the negligible decay can be observed, suggesting the excellent durability. The corresponding SEM images (inset of Fig. 4(d)) confirms that the morphology remains stable. In addition, the nanowire can be observed by OM as shown in Fig. S8 after the HER measurements, strongly confirming the adhesion of a-C/Cu$_3$P @ 400 °C on the Au-coated substrate, which proves the binder-free nature of our electrocatalysts.

All the above findings demonstrate that the a-C/Cu$_3$P @ 400 °C possess a superior HER activity with high stability, which could be attributed to the following aspects. First, the improved catalytic activity per geometric area can be achieved owing to high surface to volume ratio of peapod NWs. To confirm this part, we measured the double layer capacitance (C$_{dl}$), which is directly proportional to the electrochemical active surface area (ECSA) as shown in Fig. 5(a) where C$_{dl}$ of 2.7 mF cm^{-2} for a-C/Cu$_3$P @ 400 °C can be obtained and is higher than that of 2.1 and 1.8 mF cm^{-2} for a-C/Cu$_3$P @ 300 °C and a-C/Cu$_3$P @ 500 °C calculated from CV measurements (Fig. S9), confirming the highest surface area, leading to the lower overpotential and Tafel slope of a-C/Cu$_3$P @ 400 °C. Second, easy diffusion of the electrolyte by the peapod structure improves the direct contact to active sites of Cu$_3$P. To further evidence this phenomenon we calculated changes in Gibbs free energy of hydrogen (ΔG_{H^*}) by

Table 1
Comparison of Tafel slopes for different phosphide based samples.

Samples	Onset Potential (mV)	Tafel Slope (mV dec^{-1})	Overpotential (mV) at 10 mA cm^{-2}	Ref.
Ni$_5$P$_4$–Ni$_2$P	54	79.1	120	[21]
NiP	55	85.4	117	[69]
CoP	115	129	209	[23]
CoP NPs	NA	87	221	[70]
MoP	NA	126	105	[16]
MoP$_2$	NA	98.3	85	[71]
Cu$_3$P	145	70.2	NA	[72]
Cu$_3$P	NA	107	266	[73]
Cu–Co–P	NA	59	262	[74]
Cu$_3$P MP/CF	190	96	NA	[32]
Cu$_3$P NW/CF	62	67	143	[28]
Cu$_3$P NB/Cu	−44	72	117	[30]
Cu$_3$P/CF a-C/	100	148	222	[31]
Cu$_3$P@ 400C	211	72	287	This work

utilizing density functional theory (DFT) as presented in Fig. 5(b) where Hydrogen adsorption energy can be defined as follow:

$$\Delta E_H = \left[E_{surf+nH} - E_{surf} - (n/2)E_{H^2} \right] / n, \qquad (1)$$

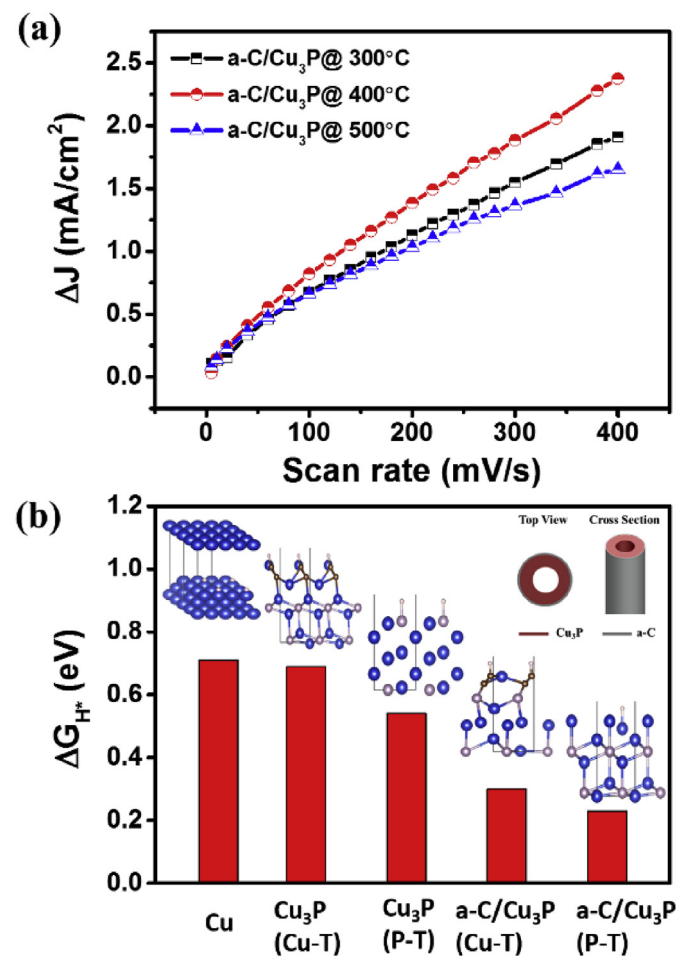where n = 1, 2 × 2 cell with the 1/6 coverage was used.

(a)

(b)

Fig. 5. (a) Measurements of double layer capacitance (C$_{dl}$) for a-C/Cu$_3$P @ 300 °C, a-C/Cu$_3$P @ 400 °C and a-C/Cu$_3$P @ 500 °C in 0.5 M H$_2$SO$_4$ at the scan rate of 5–400 mV s^{-1}. (b) The calculated free energy (ΔG$_{H^*}$) for a-C/Cu$_3$P @ 400 °C consideration with Cu- and P-terminations in comparison with single crystalline Cu.

Furthermore, Gibbs free energy can be calculated by

$$\Delta GH = \Delta EH + \Delta EZPE - T\Delta SH \qquad (2)$$

where ΔE$_H$ is hydrogen adsorption energy, ΔE$_{ZPE}$ is zero-point energy change between adsorbed and gas phase, and ΔS$_H$ is entropy difference between adsorbed and gas phase at standard conditions. For ΔE$_{ZPE}$ - TΔS$_H$, 0.29 eV was used as it is estimated from the literature [66]. The H$^+$ ions from the solution attach on the surface of nanostructures and react with the electrons to form hydrogen molecules. Therefore, changes in free energy of hydrogen imply the best catalytic behavior of an electrocatalyst where the optimal value of ΔG$_{H^*}$ is zero [67]. Because our structure posses a peapod nanowire, which can be as similar as the hollow cylinder as shown in the inset of Fig. 5(b), the outer surface of the a-C/Cu$_3$P can be as Cu-termination (Cu-T) and P-termination (P-T) whereas the Cu$_3$P with Cu-T and P-T can be the inner surface only. Therefore, the surface of the peapod NWs exhibits a complete P-T, resulting in smaller ΔG$_{H^*}$ = 0.23 eV at the outer surface and 0.54 eV at the inner surface than that of Cu-T (0.3 eV at the outer surface and 0.69 eV at the inner surface). Moreover, the calculated ΔG$_{H^*}$ for Cu-T at the inner surface is smaller than that of single crystalline Cu (0.71 eV), even higher than the reported value of polycrystalline Cu [67,68]. The a-C/Cu$_3$P @ 400 °C from the obtained lower ΔG$_{H^*}$ values asertained that the inner and outer surfaces are mostly bound with P, which is consistent with our XPS results. As a result, the Cu-T acts as hydride acceptor and the P-T acts as proton (H$^+$) acceptor at the outer surface of peapod NWs toward the electrolytes following the so-called "ensemble effect" [14]. It is well proved that the lower free energy changed at both surfaces utilize the direct contact towards the active sites (mostly P-T) and easy diffusion of electrolytes because of the peapod nanostructure. Furthermore, we demonstrated the HER experiments for non-peapod nanowires, CuP$_2$/Cu$_3$P@ 300 °C, CuP$_2$/Cu$_3$P@ 400 °C and CuP$_2$/Cu$_3$P@ 500 °C as shown in Figure S10(a). Distinctly, the achieved onset potential and overpotentials are lower than the Cu NWs, which confirm the excellent catalytic activity of Cu$_3$P due to the easy contact of the electrolyte because of the hollow core. However, the achieved overpotentials of CuP$_2$/Cu$_3$P@ 300 °C (366 mV), CuP$_2$/Cu$_3$P@ 400 °C (357 mV) and CuP$_2$/Cu$_3$P@ 500 °C (357 mV) at a current density of 10 mA cm^{-2} are all higher than that of a-C/Cu$_3$P@ 400 °C (287 mV). Moreover, CuP$_2$/Cu$_3$P@ 400 °C exhibits the unstable behavior over 1000 cycles (Figure S10b), indicating the poor HER performance owing to the absence of amorphous carbon layer and peapod shape where the Volmer-Heyrovsky mechanism is dominated confirmed by Tafel slopes (113–120 mv/dec) as shown in Figure S10(c). Finally, the dual advantages of enhanced conductivity and stability, as well as the high edge sites contributed by the hybrid a-C and a few defective graphene layers on the surface, can enhance the fast kinetic adsorption of H$^+$ during the HER confirmed by EIS measurements.

4. Conclusions

We have developed the amorphous carbon-coated Cu$_3$P peapod NWs by the CVPR at a low temperature of 400 °C that efficiently drive HER over thousands of cycles. The thick amorphous carbon layer with a few defective graphene layers serves as a protective layer and also enrich the conductivity of Cu$_3$P. The heterostructured a-C/Cu$_3$P peapod NWs exhibit a superior electrocatalytic activity by a lower overpotential of 287 mV at a current density of 10 mA cm^{-2} with a low Tafel slope of 72 mV dec^{-1} and excellent stability over 1000 cycles. The superior electrocatalytic performance can be explained by the superior contact of the electrolyte with active sites on the heterostructured a-C/Cu$_3$P due to the high surface area of

peapod NWs covered by defective edges of graphene layers with the encapsulated amorphous carbon layer. A theoretical study at the active sites of heterostructured a-C/Cu$_3$P peapod NWs by density functional theory (DFT) was proposed. Finally, how the importance of the coated a-C layer and Cu$_3$P peapod NWs were addressed, paving a feasible way to prepare an inexpensive, catalytically active and highly stable electrocatalyst for the production of excessive H$_2$ via the electrochemical water splitting process.

Acknowledgment

Appendix A. Supplementary data

Supplementary data to this article can be found online at https://doi.org/10.1016/j.electacta.2019.05.089.

References

[1] X. Zou, Y. Zhang, Noble metal-free hydrogen evolution catalysts for water splitting, Chem. Soc. Rev. 44 (2015) 5148—5180.

[2] M.-R. Gao, M.K. Chan, Y. Sun, Edge-terminated molybdenum disulfide with a 9.4-Å interlayer spacing for electrochemical hydrogen production, Nat. Commun. 6 (2015) 7493.

[3] H. Li, H. Wu, S. Yuan, H. Qian, Synthesis and characterization of vertically standing MoS2 nanosheets, Sci. Rep. 6 (2016) 21171.

[4] D. Kong, H. Wang, J.J. Cha, M. Pasta, K.J. Koski, J. Yao, Y. Cui, Synthesis of MoS2 and MoSe2 films with vertically aligned layers, Nano Lett. 13 (2013) 1341—1347.

[5] X.Y. Yu, Y. Feng, Y. Jeon, B. Guan, X.W.D. Lou, U. Paik, Formation of Ni—Co—MoS2 Nanoboxes with Enhanced Electrocatalytic Activity for Hydrogen Evolution, Advanced Materials, 2016.

[6] B. Shang, P. Ma, J. Fan, L. Jiao, Z. Liu, Z. Zhang, N. Chen, Z. Cheng, X. Cui, W. Zheng, Stabilized monolayer 1T MoS 2 embedded in CoOOH for highly efficient overall water splitting, Nanoscale 10 (2018) 12330—12336.

[7] L. Ji, L. Zhu, J. Wang, Z. Chen, Self-supported CuS nanowire array: an efficient hydrogen-evolving electrode in neutral media, Electrochim. Acta 252 (2017) 516—522.

[8] S. Czioska, J. Wang, X. Teng, Z. Chen, Hierarchically structured CuCo2S4 nanowire arrays as efficient bifunctional electrocatalyst for overall water splitting, ACS Sustain. Chem. Eng. 6 (2018) 11877—11883.

[9] H. Lin, Z. Shi, S. He, X. Yu, S. Wang, Q. Gao, Y. Tang, Heterononanowires of MoC—Mo 2 C as efficient electrocatalysts for hydrogen evolution reaction, Chem. Sci. 7 (2016) 3399—3405.

[10] C. Lu, D. Tranca, J. Zhang, F.n. Rodrıguez Hernández, Y. Su, X. Zhuang, F. Zhang, G. Seifert, X. Feng, Molybdenum carbide-embedded nitrogen-doped porous carbon nanosheets as electrocatalysts for water splitting in alkaline media, ACS Nano 11 (2017) 3933—3942.

[11] Y. Zheng, Y. Jiao, LH. Li, T. Xing, Y. Chen, M. Jaroniec, S.Z. Qiao, Toward design of synergistically active carbon-based catalysts for electrocatalytic hydrogen evolution, ACS Nano 8 (2014) 5290—5296.

[12] R. Li, L. Yang, T. Xiong, Y. Wu, L. Cao, D. Yuan, W. Zhou, Nitrogen doped MoS2 nanosheets synthesized via a low-temperature process as electrocatalysts with enhanced activity for hydrogen evolution reaction, J. Power Sources 356 (2017) 133—139.

[13] H. Zhang, Z. Ma, J. Duan, H. Liu, G. Liu, T. Wang, K. Chang, M. Li, L. Shi, X. Meng, Active sites implanted carbon cages in core—shell architecture: highly active and durable electrocatalyst for hydrogen evolution reaction, ACS Nano 10 (2016) 684—694.

[14] P. Liu, J.A. Rodriguez, Catalysts for hydrogen evolution from the [NiFe] hydrogenase to the Ni2P (001) surface: the importance of ensemble effect, J. Am. Chem. Soc. 127 (2005) 14871—14878.

[15] P. Liu, J.A. Rodriguez, T. Asakura, J. Gomes, K. Nakamura, Desulfurization reactions on Ni2P (001) and α-Mo2C (001) surfaces: complex role of P and C sites, J. Phys. Chem. B 109 (2005) 4575—4583.

[16] C. Deng, F. Ding, X. Li, Y. Guo, W. Ni, H. Yan, K. Sun, Y.-M. Yan, Templated-preparation of a three-dimensional molybdenum phosphide sponge as a high performance electrode for hydrogen evolution, J. Mater. Chem. 4 (2016) 59—66.

[17] P. Xiao, M.A. Sk, L. Thia, X. Ge, R.J. Lim, J.-Y. Wang, K.H. Lim, X. Wang, Molybdenum phosphide as an efficient electrocatalyst for the hydrogen evolution

[18] Z. Xing, Q. Liu, A.M. Asiri, X. Sun, Closely interconnected network of molybdenum phosphide nanoparticles: a highly efficient electrocatalyst for generating hydrogen from water, Adv. Mater. 26 (2014) 5702—5707.

[19] Y. Pan, Y. Liu, J. Zhao, K. Yang, J. Liang, D. Liu, W. Hu, D. Liu, Y. Liu, C. Liu, Monodispersed nickel phosphide nanocrystals with different phases: synthesis, characterization and electrocatalytic properties for hydrogen evolution, J. Mater. Chem. 3 (2015) 1656—1665.

[20] T. Tian, L. Ai, J. Jiang, Metal—organic framework-derived nickel phosphides as efficient electrocatalysts toward sustainable hydrogen generation from water splitting, RSC Adv. 5 (2015) 10290—10295.

[21] X. Wang, Y.V. Kolen'ko, X.Q. Bao, K. Kovnir, L. Liu, One-step synthesis of self-supported nickel phosphide nanosheet array cathodes for efficient electrocatalytic hydrogen generation, Angew. Chem. 127 (2015) 8306—8310.

[22] S. Czioska, J. Wang, S. Zuo, X. Teng, Z. Chen, Hierarchically structured NiFeOx/CuO nanosheets/nanowires as an efficient electrocatalyst for the oxygen evolution reaction, ChemCatChem 10 (2018) 1005—1011.

[23] J. Tian, Q. Liu, A.M. Asiri, X. Sun, Self-supported nanoporous cobalt phosphide nanowire arrays: an efficient 3D hydrogen-evolving cathode over the wide range of pH 0—14, J. Am. Chem. Soc. 136 (2014) 7587—7590.

[24] Y. Pan, Y. Liu, Y. Lin, C. Liu, Metal doping effect of the M—Co2P/Nitrogen-Doped carbon nanotubes (M= Fe, Ni, Cu) hydrogen evolution hybrid catalysts, ACS Appl. Mater. Interfaces 8 (2016) 13890—13901.

[25] E.J. Popczun, C.G. Read, C.W. Roske, N.S. Lewis, R.E. Schaak, Highly active electrocatalysis of the hydrogen evolution reaction by cobalt phosphide nanoparticles, Angew. Chem. Int. Ed. 53 (2014) 5427—5430.

[26] C. Lv, Z. Peng, Y. Zhao, Z. Huang, C. Zhang, The hierarchical nanowires array of iron phosphide integrated on a carbon fiber paper as an effective electrocatalyst for hydrogen generation, J. Mater. Chem. 4 (2016) 1454—1460.

[27] L. Tian, X. Yan, X. Chen, Electrochemical activity of iron phosphide nanoparticles in hydrogen evolution reaction, ACS Catal. 6 (2016) 5441—5448.

[28] J.F. Callejas, J.M. McEnaney, C.G. Read, J.C. Crompton, A.J. Biacchi, E.J. Popczun, T.R. Gordon, N.S. Lewis, R.E. Schaak, Electrocatalytic and photocatalytic hydrogen production from acidic and neutral-pH aqueous solutions using iron phosphide nanoparticles, ACS Nano 8 (2014) 11101—11107.

[29] A. Han, H. Zhang, R. Yuan, H. Ji, P. Du, Crystalline copper phosphide nanosheets as an efficient janus catalyst for overall water splitting, ACS Appl. Mater. Interfaces 9 (2017) 2240—2248.

[30] S. Wei, K. Qi, Z. Jin, J. Cao, W. Zheng, H. Chen, X. Cui, One-step synthesis of a self-supported copper phosphide nanobush for overall water splitting, ACS Omega 1 (2016) 1367—1373.

[31] C.-C. Hou, Q.-Q. Chen, C.-J. Wang, F. Liang, Z. Lin, W.-F. Fu, Y. Chen, Self-supported cedarlike semimetallic Cu3P nanoarrays as a 3D high-performance janus electrode for both oxygen and hydrogen evolution under basic conditions, ACS Appl. Mater. Interfaces 8 (2016) 23037—23048.

[32] J. Tian, Q. Liu, N. Cheng, A.M. Asiri, X. Sun, Self-supported Cu3P nanowire arrays as an integrated high-performance three-dimensional cathode for generating hydrogen from water, Angew. Chem. Int. Ed. 53 (2014) 9577—9581.

[33] C. Lu, J. Wang, S. Czioska, H. Dong, Z. Chen, Hierarchically structured Cu-based electrocatalysts with nanowires array for water splitting, J. Phys. Chem. C 121 (2017) 25875—25881.

[34] R. Wang, X.Y. Dong, J. Du, J.Y. Zhao, S.Q. Zang, MOF-Derived bifunctional Cu3P nanoparticles coated by a N, P-codoped carbon shell for hydrogen evolution and oxygen reduction, Adv. Mater. 30 (2018) 1703711.

[35] E.A. Lewis, W.B. Tolman, Reactivity of dioxygen— copper systems, Chem. Rev. 104 (2004) 1047—1076.

[36] A. Manikandan, L. Lee, Y.-C. Wang, C.-W. Chen, Y.-Z. Chen, H. Medina, J.-Y. Tseng, Z.M. Wang, Y.-L. Chueh, Graphene-coated copper nanowire networks as a highly stable transparent electrode in harsh environments toward efficient electrocatalytic hydrogen evolution reactions, J. Mater. Chem. 5 (2017) 13320—13328.

[37] X. Zhao, H. Zhu, X. Yang, Amorphous carbon supported MoS 2 nanosheets as effective catalysts for electrocatalytic hydrogen evolution, Nanoscale 6 (2014) 10680—10685.

[38] D. Merki, H. Vrubel, L. Rovelli, S. Fierro, X. Hu, Fe, Co, and Ni ions promote the catalytic activity of amorphous molybdenum sulfide films for hydrogen evolution, Chem. Sci. 3 (2012) 2515—2525.

[39] G. Manna, R. Bose, N. Pradhan, Semiconducting and plasmonic copper phosphide platelets, Angew. Chem. 125 (2013) 6894—6898.

[40] L. De Trizio, R. Gaspari, G. Bertoni, I. Kriegel, L. Moretti, F. Scotognella, L. Maserati, Y. Zhang, G.C. Messina, M. Prato, Cu3-x P nanocrystals as a material platform for near-infrared plasmonics and cation exchange reactions, Chem. Mater. 27 (2015) 1120—1128.

[41] D. Sun, X. Zhu, B. Luo, Y. Zhang, Y. Tang, H. Wang, L. Wang, New binder-free metal phosphide—carbon felt composite anodes for sodium-ion battery, Adv. Energy Mater. (2018) 1801197.

[42] G. Kresse, J. Furthmüller, Efficient iterative schemes for ab initio total-energy calculations using a plane-wave basis set, Phys. Rev. B 54 (1996) 11169.

[43] P.E. Blöchl, Projector augmented-wave method, Phys. Rev. B 50 (1994) 17953.

[44] J.P. Perdew, K. Burke, M. Ernzerhof, Generalized gradient approximation made simple, Phys. Rev. Lett. 77 (1996) 3865.

[45] H.J. Monkhorst, J.D. Pack, Special points for Brillouin-zone integrations, Phys. Rev. B 13 (1976) 5188.

[46] P.E. Blöchl, O. Jepsen, O.K. Andersen, Improved tetrahedron method for

Brillouin-zone integrations, Phys. Rev. B 49 (1994) 16223.

[47] A.C. Ferrari, J. Robertson, Interpretation of Raman spectra of disordered and amorphous carbon, Phys. Rev. B 61 (2000) 14095.

[48] J. Fu, H. Qiao, D. Li, L. Luo, K. Chen, Q. Wei, Laccase biosensor based on electrospun copper/carbon composite nanofibers for catechol detection, Sensors 14 (2014) 3543—3556.

[49] X. Wang, K. Han, Y. Gao, F. Wan, K. Jiang, Fabrication of novel copper phosphide (Cu 3 P) hollow spheres by a simple solvothermal method, J. Cryst. Growth 307 (2007) 126—130.

[50] S. Lee, J. Hong, J.H. Koo, H. Lee, S. Lee, T. Choi, H. Jung, B. Koo, J. Park, H. Kim, Synthesis of few-layered graphene nanoballs with copper cores using solid carbon source, ACS Appl. Mater. Interfaces 5 (2013) 2432—2437.

[51] Y.-Z. Chen, H. Medina, H.-W. Tsai, Y.-C. Wang, Y.-T. Yen, A. Manikandan, Y.-L. Chueh, Low temperature growth of graphene on glass by carbon-enclosed chemical vapor deposition process and its application as transparent electrode, Chem. Mater. 27 (2015) 1646—1655.

[52] H. Xu, H. Wang, C. Wu, N. Lin, A.M. Soomro, H. Guo, C. Liu, X. Yang, Y. Wu, D. Cai, Direct synthesis of graphene 3D-coated Cu nanosilks network for antioxidant transparent conducting electrode, Nanoscale 7 (2015) 10613—10621.

[53] S. Liu, X. He, J. Zhu, L. Xu, J. Tong, Cu 3 P/RGO nanocomposite as a new anode for lithium-ion batteries, Sci. Rep. 6 (2016) 35189.

[54] Y. Kim, Y. Park, A. Choi, N.S. Choi, J. Kim, J. Lee, J.H. Ryu, S.M. Oh, K.T. Lee, An amorphous red phosphorus/carbon composite as a promising anode material for sodium ion batteries, Adv. Mater. 25 (2013) 3045—3049.

[55] L. Wang, X. He, J. Li, W. Sun, J. Gao, J. Guo, C. Jiang, Nano-Structured phosphorus composite as high-capacity anode materials for lithium batteries, Angew. Chem. Int. Ed. 51 (2012) 9034—9037.

[56] S. Bae, H. Kim, Y. Lee, X. Xu, J.-S. Park, Y. Zheng, J. Balakrishnan, T. Lei, H.R. Kim, Y.I. Song, Roll-to-roll production of 30-inch graphene films for transparent electrodes, Nat. Nanotechnol. 5 (2010) 574—578.

[57] J. Du, J. Wang, L. Ji, X. Xu, Z. Chen, A highly active and robust copper-based electrocatalyst toward hydrogen evolution reaction with low overpotential in neutral solution, ACS Appl. Mater. Interfaces 8 (2016) 30205—30211.

[58] Y.-C. Chen, Z.-B. Chen, Y.-G. Lin, Y.-K. Hsu, Synthesis of copper phosphide nanotube arrays as electrodes for asymmetric supercapacitors, ACS Sustain. Chem. Eng. 5 (2017) 3863—3870.

[59] L. Wei, K. Goh, Ö. Birer, H.E. Karahan, J. Chang, S. Zhai, X. Chen, Y. Chen, A hierarchically porous nickel—copper phosphide nano-foam for efficient electrochemical splitting of water, Nanoscale 9 (2017) 4401—4408.

[60] Y.-Z. Chen, H. Medina, H.-C. Lin, H.-W. Tsai, T.-Y. Su, Y.-L. Chueh, Large-scale and patternable graphene: direct transformation of amorphous carbon film into graphene/graphite on insulators via Cu mediation engineering and its application to all-carbon based devices, Nanoscale 7 (2015) 1678—1687.

[61] Q. Guan, W. Li, A novel synthetic approach to synthesizing bulk and supported

[62] M. Losurdo, M.M. Giangregorio, P. Capezzuto, G. Bruno, Graphene CVD growth on copper and nickel: role of hydrogen in kinetics and structure, Phys. Chem. Chem. Phys. 13 (2011) 20836—20843.

[63] K. Wang, J. Yang, J. Xie, B. Wang, Z. Wen, Electrochemical reactions of lithium with CuP2 and Li1. 75Cu1. 25P2 synthesized by ballmilling, Electrochem. Commun. 5 (2003) 480—483.

[64] X. Chen, G. Liu, W. Zheng, W. Feng, W. Cao, W. Hu, P. Hu, Vertical 2D MoO2/MoSe2 core—shell nanosheet arrays as high-performance electrocatalysts for hydrogen evolution reaction, Adv. Funct. Mater. 26 (2016) 8537—8544.

[65] A. Manikandan, P.R. Ilango, C.-W. Chen, Y.-C. Wang, Y.-C. Shih, L. Lee, Z.M. Wang, H. Ko, Y.-L. Chueh, A superior dye adsorbent towards the hydrogen evolution reaction combining active sites and phase-engineering of (1T/2H) MoS 2/α-MoO 3 hybrid heterostructured nanoflowers, J. Mater. Chem. 6 (2018) 15320—15329.

[66] B. Hinnemann, P.G. Moses, J. Bonde, K.P. Jørgensen, J.H. Nielsen, S. Horch, I. Chorkendorff, J.K. Nørskov, Biomimetic hydrogen evolution: MoS2 nanoparticles as catalyst for hydrogen evolution, J. Am. Chem. Soc. 127 (2005) 5308—5309.

[67] Y. Zheng, Y. Jiao, M. Jaroniec, S.Z. Qiao, Advancing the electrochemistry of the hydrogen-evolution reaction through combining experiment and theory, Angew. Chem. Int. Ed. 54 (2015) 52—65.

[68] Y. Zheng, Y. Jiao, Y. Zhu, L.H. Li, Y. Han, Y. Chen, A. Du, M. Jaroniec, S.Z. Qiao, Hydrogen evolution by a metal-free electrocatalyst, Nat. Commun. 5 (2014).

[69] X. Wang, W. Li, D. Xiong, D.Y. Petrovykh, L. Liu, Bifunctional nickel phosphide nanocatalysts supported on carbon fiber paper for highly efficient and stable overall water splitting, Adv. Funct. Mater. 26 (2016) 4067—4077.

[70] P. Jiang, Q. Liu, C. Ge, W. Cui, Z. Pu, A.M. Asiri, X. Sun, CoP nanostructures with different morphologies: synthesis, characterization and a study of their electrocatalytic performance toward the hydrogen evolution reaction, J. Mater. Chem. 2 (2014) 14634—14640.

[71] W. Zhu, C. Tang, D. Liu, J. Wang, A.M. Asiri, X. Sun, A self-standing nanoporous MoP 2 nanosheet array: an advanced pH-universal catalytic electrode for the hydrogen evolution reaction, J. Mater. Chem. 4 (2016) 7169—7173.

[72] L. Ma, X. Shen, H. Zhou, J. Zhu, C. Xi, Z. Ji, L. Kong, Synthesis of Cu 3 P nanocubes and their excellent electrocatalytic efficiency for the hydrogen evolution reaction in acidic solution, RSC Adv. 6 (2016) 9672—9677.

[73] H. Wang, T. Zhou, P. Li, Z. Cao, W. Xi, Y. Zhao, Y. Ding, Self-supported hierarchical nanostructured NiFe-LDH and Cu3P weaving mesh electrodes for efficient water splitting, ACS Sustain. Chem. Eng. 6 (2017) 380—388.

[74] R.N. Wasalathanthri, S. Jeffrey, R.A. Awni, K. Sun, D.M. Giolando, Electrodeposited copper—cobalt—phosphide: a stable bifunctional catalyst for both hydrogen and oxygen evolution reactions, ACS Sustain. Chem. Eng. 7 (2018) 3092—3100.